49th AIAA Aerospace Sciences Meeting including the New Horizons Forum and Aerospace Exposition
4 - 7 January 2011, Orlando, Florida

AIAA 2011-910

Modeling of Wedge-Shaped Porous Flaps for Jet Noise Reduction

Juntao Xiong[1], Andrew D. Johnson[2], Feng Liu[3], and Dimitri Papamoschou[4]
University of California, Irvine, CA 92697, USA

This article presents experimental and computational analyses of the flow field associated with porous wedge-shaped deflectors used for jet noise reduction in turbofan engines. The goal is to characterize the key parameters affecting the flow field in order to construct a macroscopic computational model of the deflector that obviates resolution of its detailed perforations. The model simulates the effects of the inclined porous surfaces by applying locally a body force term in the conservation equations. The investigation encompassed wedge deflectors, in the form of flaps, with varying angles and different perforation shapes. The experiments measured the mean velocity field inside and in the wake of the flaps. The numerical effort comprised direct computations of simplified perforations and approximate computations using the body force model. It is found that the flow field is affected not only by the porosity of the deflectors but also by the illumination angle defined by the shape and thickness of the perforation. A formulation for the body force model is proposed that incorporates this finding. The resulting velocity field is in good agreement with the experiments and with the direct computations.

Nomenclature

AR	=	perforation aspect ratio
C	=	inertial resistance coefficient
C_p	=	pressure coefficient
D	=	hole diameter
F_B	=	locally applied body force
H	=	nozzle height
h	=	flap height
L	=	flap length
M_∞	=	freestream Mach number
NPR	=	nozzle pressure ratio
p_a	=	ambient pressure
p_{res}	=	reservoir pressure
U_∞	=	freestream velocity
u,v,w	=	components of mean velocity
W	=	nozzle width
α	=	wedge half-angle
β	=	porosity
t	=	flap thickness
θ_i	=	illumination angle
v_n	=	permeation velocity

[1] Post Doctoral Researcher, Department of Mechanical and Aerospace Engineering, jxiong@uci.edu, AIAA Member.
[2] Post Doctoral Researcher, Department of Mechanical and Aerospace Engineering, adjohnso@uci.edu, AIAA Member.
[3] Professor, Department of Mechanical and Aerospace Engineering, fliu@uci.edu, AIAA Associate Fellow.
[4] Professor, Department of Mechanical and Aerospace Engineering, dpapamos@uci.edu, AIAA Fellow.

I. Introduction

RECENT efforts in jet noise reduction for turbofan nozzles have focused on reshaping the exhaust plume in such a way as to provide directional noise suppression.[1,2] One such approach utilizes wedge-shaped fan flow deflectors, as illustrated in Fig. 1. The role of the deflector is to direct some of the fan stream underneath the core stream, thus reducing velocity gradients and turbulent kinetic energy (TKE) production on the underside of the jet. Wedge-shaped fan flow deflectors have been studied for low- and high-bypass configurations,[2-4] as well as in propulsion-airframe integration concepts for jet noise shielding.[5] Figure 2 shows a typical noise reduction trend. Porous wedge deflectors have superior aerodynamic features that enhance their potential as noise reduction devices. The goal of this study is the development of methodologies for the efficient aerodynamic computation of porous deflectors. This section provides some important background into the aerodynamics of fan flow deflector (FFD) wedges.

The upper side of the FFD wedge is exposed to the ambient environment, resulting in significant aerodynamic differences from the classic flow around a fully immersed, two-dimensional wedge.[6] Past experiments on large-scale FFD wedges have shown the local flow field to be highly three-dimensional with a strong localized upwash.[7] This behavior is explained using inviscid treatment of the flow approaching the wedge apex, as illustrated on the diagram of Fig. 3. The free streamline exiting the nozzle and approaching the apex must conserve the magnitude of velocity ($C_p = 0$). At the apex, the u and w components of velocity are stagnated due to symmetry conditions thus causing the v (upward) component of velocity to approach the freestream velocity, U_∞. This is evident in the flow visualization on the photograph of Fig. 3 by the almost vertical streak lines near the top of the wedge apex.

Figure 4 compares the pressure distribution on the surface of a solid FFD wedge versus a classic two-dimensional wedge. The classic wedge shows a compression followed by suction along the side surface, resulting in a negligible side force. In contrast, the FFD wedge shows a compression over the entire side surface producing a finite side force. Also, the classic wedge has a strong negative base pressure ($C_p \approx -1.0$) compared to the much weaker base pressure of the FFD wedge ($C_p \approx -0.2$). As a result, the drag of the FFD wedge is roughly 25% that of the fully-immersed 2D wedge.[7]

Practical implementation of this method would likely involve deployed flaps, activated when noise reduction is desired and retracted otherwise. This would confine performance penalties to the noise-sensitive flight segments. Utilizing porous flaps, as opposed to solid flaps, allows some flow to penetrate the wedge-shaped deflector.[4] This alleviates excessive velocity gradients in the core stream at the base of the wedge that can cause localized strong noise sources. The deflector self-noise influences mainly the large polar angles from the jet axis and can be strong enough to reduce and even reverse the perceived-noise benefits stemming from the downward reduction in TKE. Subscale experiments at U.C. Irvine have shown consistent noise benefits of porous flaps over solid flaps or wedges, for subsonic and supersonic engine cycles. Porosities of about 50% are deemed optimal. In addition to the noise benefit of the porous deflector, drag is expected to be reduced by as much 50% from the solid case.[4]

While having favorable performance characteristics, the porous surfaces introduce challenges for the computational modeling of the flow field. The geometric complexity of the perforation makes resolving the actual fluid interaction at the porous surface unrealistic. Therefore, approximate methods must be developed that have an analogous effect on the flow field. The purpose of this investigation is to combine experimental evidence with feasible simulations of wedges of simplified perforations to identify key parameters effecting flow through and around the porous boundaries. This information is then used to formulate a useful model for conducting large-scale fully three-dimensional simulations of nozzles with porous wedge-shape deflector geometries.

II. Experimental Effort

A. Nozzle and Deflector Description

Experiments are used here both as an investigative tool as well as a means of comparison and validation with computation results. Acoustic experiments conducted on subscale models of turbofan exhaust nozzles (approximately $1/50^{th}$ the scale of an actual engine) involved flap dimensions on the order of just millimeters. At this scale, detailed flow measurements in the vicinity of the wedge are rather difficult to obtain and are unreliable for comparison with computational data. For this reason, a scaled-up experiment was devised with larger flaps mounted near the exit of an existing high aspect ratio planar nozzle. This provided an approximate flow field to the one in the vicinity of the wedge mounted outside a fan nozzle with a sufficiently large radius of curvature compared to its exit height as illustrated in Fig. 5. The planar nozzle used here was originally designed for the study of nozzle flow separation.

The upper and lower walls of the nozzle can be flexed to achieve convergent-divergent, convergent, or straight contours. In these experiments the walls terminate straight with an exit height of H = 17.78 mm and a width of W = 65 mm. A full description of the nozzle facility can be found in Ref. 8. The nozzle is connected to a pressure regulated air supply that can deliver nozzle pressure ratios up to NPR = p_{res}/p_a = 3.5. The nozzle pressure ratios considered in this study were NPR = 1.2, 1.6 and 2.0. The corresponding fully-expanded velocities were U_∞=172.5, 271.5, and 324.6 m/s, respectively.

The flaps used to make up the wedge-shaped deflector have a length of L = 50 mm and a height of h = 28 mm (approximately five times larger than the subscale turbofan experiments). The flap thickness, t, as well as the shape of the perforations could be varied. Custom perforation designs were manufactured using laser cutting. Round holes (hole aspect ratio AR=1.0) were tested as well as holes that were lengthened in the streamwise direction to an aspect ratio of AR = 3.0. The porosity of the flaps could be varied between β = 0.0 (solid flaps) to β = 1.0 (no flaps). Experiments have shown that a porosity of around 50% tends to yield superior acoustic results.[4] The flaps were inserted into slots on the adjacent wall surface aligned with the bottom wall of the planar nozzle with the apex of the wedge situated at 20 mm from the nozzle exit. The slots were cut to allow wedge half-angles of α = 20°, 30°, or 40°. A top-view of the wall surface is illustrated in Fig. 6 with flaps inserted at α = 30°. A photograph of the setup is shown in Fig. 7. The Reynolds number $U_\infty L/\nu$ ranged from 6.28×10^5 (NPR=1.2) to 1.54×10^6 (NPR=2.0).

B. Mean Wake Surveys

The mean total pressure in the wake of the wedge was surveyed using a Pitot rake system. The rake consists of five 70 mm long probes with 0.5-mm internal diameters and are vertically spaced 10 mm apart using a streamlined mounting plate. Each Pitot probe is connected individually to a Setra Model 207 pressure transducer. The rake is attached to a three dimensional traverse system consisting of three IMS MDrive 23 motor drivers connected individually to THK LM Guide Actuators. The traverse system is remotely controlled using National Instruments LabView. A pre-specified traverse path was given to the control program, generally consisting of scans of five axial planes (x/L = 0.5, 1.0, 1.5, 2.5, and 3.5) measured from the wedge apex. Note that the first axial station was inside the wedge. The positions y/L = 0.0 and z/L = 0.0 correspond to the vertical and spanwise centerplanes of the nozzle.

The data on each y-z plane are interpolated on a fixed grid. The total pressure measured by each Pitot probe is converted to velocity under the assumption of constant static pressure (equal to the ambient value) and constant total temperature (equal to room temperature). This is a reasonable assumption in the case of an FFD wedge because the top side of the wedge is exposed to ambient pressure.

III. Computational Effort

The computations simulated the experimental conditions of the previous section, except for the details of the perforations. Because it is unfeasible to compute the detailed flow field of the hundreds of perforations in the experimental setup, the numerical effort made two approximations: direct computation of a very coarse perforation; and simulation of the effect of the perforation using a body force term in the momentum equation.

A. Direct Computation

Direct computations were performed for very coarse perforations (~10 holes per flap) with the same porosity, aspect ratio, and ratio of thickness to hole size as in the experiments. The purpose of these computations was to gain insight into the detailed flow interactions, particularly in the interior of the wedge. The geometries and grids of the wedges are shown in Fig. 9. Approximately 9 million grid points were used for each configuration.

B. Simulation using Body Force Term

The effect of a solid or porous surface can be modeled by implementing a body force term in the Navier-Stokes equations:

$$\frac{\partial(\rho\vec{u})}{\partial t} + \nabla\cdot(\rho\vec{u}\vec{u}) = -\nabla p + \nabla\cdot\bar{\bar{\tau}} - \vec{F}_B \tag{1}$$

The $\vec{F}_B$ term is applied locally at the porous media cells and generates a momentum sink that corresponds to a pressure drop across the boundary. The pressure drop across a porous medium can be represented by the sum of a viscous loss term proportional to the normal or permeation velocity v_n and an inertial loss term proportional to the square of the permeation velocity.[9] The Reynolds numbers of the flows considered here are sufficiently high to justify neglecting the viscous loss term, resulting in the formulation

$$\vec{F}_B = \frac{1}{2}\rho C\left|\vec{v}_n\right|\vec{v}_n \tag{2}$$

where C is a dimensional coefficient called the inertial resistance coefficient. For a porous plate normal to a flow, the inertial resistance coefficient is primarily a function of porosity.[10]

As a first approximation, the inertial resistance coefficient was obtained by calibrating the model against experimental measurements of drag coefficient for a perforated plate inclined normal to a freestream.[11] The coefficient of drag is plotted versus porosity in Fig. 10 for the referenced experiment and the computation utilizing the body force model. The trend is reproduced well using the body force model and shows a nearly linear decay in drag coefficient with increasing porosity.

When the porous surface is inclined to the freestream, such as in the case of the wedge deflector, the model yields unsatisfactory results. This suggests that additional variables, beyond porosity, should be included in the definition of the inertial resistance coefficient C. The central goal of this study is to identify those additional parameters and reformulate the body force model accordingly.

C. Numerical Details

The computational fluid dynamics code used here is known as ParCAE and solves the unsteady three-dimensional Reynolds-averaged Navier-Stokes (RANS) equations on structured multi-block grids using a cell centered finite-volume method with artificial dissipation as proposed by Jameson et al.[12] Information exchange for flow computation on multi-block grids using multiple CPUs is implemented through the MPI (message passing interface) protocol. The RANS equations are solved using the shear stress transport (SST) turbulence model by Menter.[13] In this study, only the steady-state solution is considered because we are interested in the time-averaged features of the flow. A low ambient Mach number (M_a = 0.05) with preconditioning was applied to the computational domain to prevent numerical singularities from arising. A more thorough description of the computational code is provided in Ref. 14. The computational domain is depicted in Fig.11.

The code treats each block as a separate entity and therefore only the flow and turbulence quantities need be exchanged at the block boundaries. The governing equations are solved explicitly in a coupled manner using a five-stage Runge-Kutta scheme toward steady-state with local-time stepping, residual smoothing and multigrid techniques for convergence acceleration. Futher details of the numerical method can be found in Ref. 15.

IV. Results

A. Experimental Results

Mean axial velocity contours at the first three axial stations for the undeflected case with no wedge present (β = 1.0) and nozzle pressure ratio of NPR = 1.6 are shown in Fig. 12(a). The mean velocity has been normalized by the perfectly expanded jet exit velocity, U_∞. The first axial station is located at a distance of 0.9L from the exit of the nozzle, corresponding to x/L = 0.5 from where the apex of the wedge would be located. The flow develops normally downstream with mixing primarily occurring on the upper and side boundaries due to the confinement of the jet by the lower wall surface in the near field. The boundary layer above the wall surface is not resolved in these experiments. While the probe tips are hypodermic, they have tapered lengths requiring the measurement point to be at a finite distance from the wall.

The same plots are shown in Fig. 12(b) with porous flaps (β = 0.5) inserted at a half angle of $\alpha = 30^o$. The perforations are round with flap thickness to hole diameter ratio of t/D = 0.45. The flow field is dramatically different, showing evidence of a strong sideward deflection with the upwash characteristics described in the introduction. The asymmetry of the flow field, particularly noticeable downstream in the third axial plane, suggests the flow is rather sensitive to subtle asymmetry in the wedge geometry. The flow asymmetry appears to be perpetuated by the development of streamwise vortices generated over the upper edge of the flaps. The flow penetrating through the porous surfaces coalesces into a centered jet rather than the more uniform distribution that was expected. Contrary to the intent of utilizing porous flaps, this can generate additional velocity gradients downstream of the wedge rather than smoothing those which were already present. In terms of noise production, this is a negative characteristic.

Figure 13(a-c) shows the mean velocity contour at the second axial station x/L = 1.0 (just behind the wedge base) for three different nozzle pressure ratios NPR = 1.2, 1.6, and 2.0. The normalized velocity contours look nearly identical, aside from subtle differences in the flow penetrating through the porous flaps. This suggests that the

velocity through and around the porous flap scales with the freestream velocity (in this case, the perfectly expanded nozzle exit velocity). Furthermore, the inertial resistance through the flap shows little dependence on nozzle pressure ratio. The flow through the porous wedge in Fig. 13 is not only nonuniform but also relatively weak in magnitude. This suggests that at this shallow angle to the freestream, flow through the porous surface is nearly closed off. The effect of increasing the wedge half-angle is seen in Fig. 14(a-c) for NPR = 1.2. As the angle is increased from α = 20^o to α = 40^o, substantially more flow penetrates through the wedge.

Figure 15 compares two cases with the same porosity β = 0.5 and half angle α = 20^o but the aspect ratio of the holes differs by a factor of three in the streamwise direction (AR = 1.0 versus AR = 3.0). The AR = 1.0 wedge is depicted in Fig. 6(a) and the AR = 3.0 wedge in Fig. 6(b). At NPR = 1.2, the higher-aspect-ratio holes result in less of an upwash in the deflected flow and instead a dramatic increase of the flow through the porous wedge. The peak magnitude more than doubles and the distribution is more uniform.

Figures 14 and 15 suggest that the flow field is dependent not only on porosity but also on the "see through" or illumination angle. The illumination angle θ_i is defined by the diagram of Fig.16. With the freestream velocity used as the reference velocity, the illumination angle is

$$\theta_{i\infty} = \alpha - \arctan\left(\frac{t}{D}\right) \tag{3}$$

Increasing the flap angle, hole diameter-to-thickness ratio, or hole aspect ratio in the streamwise direction, will result in an increased illumination angle. Positive illumination angle means that the flow has a direct path across the perforation. Negative illumination angle means that direct access is blocked. For very negative illumination angles we expect that flow through the perforation is driven primarily by pressure.

B. Computations with Simplified Perforations

Figure 17 compares experimental results with computational results for flow about a porous wedge with a half-angle of α = 20^o and with the same porosity and freestream illumination angle (β = 0.5 and $\theta_{i\infty}$ = -4^o). The geometry of the computational wedge, shown in Fig. 9(a), differs from the experimental geometry in that it has been greatly simplified to reduce computational cost. The number of holes is greatly reduced and the shape is rectangular instead of round. Despite the obvious geometric difference, simply matching the porosity and illumination angle yields good agreement in the mean velocity field downstream. At this negative illumination angle, both results show a relatively weak and centered distribution penetration flow near the wedge base (x/L = 1.0).

Similar agreement between experiment and computation is shown in the results for a positive freestream illumination angle of $\theta_{i\infty}$ = 12^o in Fig. 18. The computational wedge geometry with an increased streamwise aspect ratio is depicted in Fig. 9(b). Switching from a negative to a positive illumination angle causes an overall increase in the magnitude of velocity of the flow through the porous surface. The computational results match quite well with the levels observed in the experiment. In both cases, the experimental distribution is smoother since the smaller hole size allows for more rapid mixing of the flow downstream.

The computations provide interesting details about the physics of the flow passing through the perforations. Figure 19 shows the mean axial velocity contours in the *x*-*z* plane for both negative and positive illumination angles. If the freestream illumination angle is negative, there is clearly no direct path for the incoming flow to pass directly through the surface as seen in Fig 19(a). Instead, the flow is driven only by the pressure difference across the surface. This correlates to a penetration velocity that is relatively low in magnitude and nearly normal to the surface, causing the formation of a center jet downstream. If the freestream illumination angle is positive, there is a direct path for incident flow to pass through the surface as seen in Fig. 19(b). This allows the penetrating flow to retain a higher magnitude and also reduces the inward turning of the flow resulting in a more uniform profile downstream.

C. Body Force Model Formulation and Validation

The experimental results as well as the computations on simplified perforated geometry suggest that the revised body force model must have an explicit dependence on not only the porosity, but also the illumination angle. Furthermore, the agreement in the previous section suggests that if these two quantities are accounted for, the body force model should yield an accurate approximation regardless of other geometric details such as hole shape.

In the revised model, a porous surface inclined at an arbitrary angle to the freestream flow is locally decomposed into three orthogonal porous surfaces inclined normal to the *u*, *v*, and *w* components of local velocity vector. The body force applied to Eq. 1 is then written as the sum of the forces generated by each surface component:

$$\vec{F}_B = \frac{1}{2}\rho\left(C_x|u|u\hat{e}_x + C_y|v|v\hat{e}_y + C_z|w|w\hat{e}_z\right) \tag{4}$$

In the case of the porous wedge deflector, the finite thickness of the flap realistically would cause some resistance to the *v* component of velocity through the surface. However, for simplicity the contribution of the body force in the *y*-direction is neglected on the basis that the flap is relatively thin. The inertial resistance coefficients can be written as a function of the effective porosity in each direction

$$C_x = \Psi\left(\beta_{eff,x}\right) \quad \text{and} \quad C_z = \Psi\left(\beta_{eff,z}\right) \tag{5}$$

Assuming rectangular perforations with width D and height δ, the porosity is written

$$\beta = \frac{ND\delta}{hL} \tag{6}$$

where N is the number of holes. Following the diagram in Fig. 16, the effective porosity in the *x*-direction is similarly

$$\beta_{eff,x} = \frac{N\left(\sqrt{D^2 + t^2}\,\sin\theta_{ix}\right)\delta}{hL\sin\alpha} \tag{7}$$

where θ_{ix} is illumination angle with respect to the *u* component of velocity and is identical to the illumination angle defined with respect to the freestream velocity $\theta_{ix} = \theta_{i\infty}$. Combining Eqs. 6 and 7, the effective porosity in the *x*-direction can be written as

$$\beta_{eff,x} = \beta\frac{\sin\theta_{ix}}{\sin\alpha}\sqrt{1+\left(\frac{t}{D}\right)^2} \tag{8}$$

Similarly, in the *z*-direction we have

$$\beta_{eff,z} = \beta\frac{\sin\theta_{iz}}{\cos\alpha}\sqrt{1+\left(\frac{t}{D}\right)^2} \tag{9}$$

where θ_{iz} is the illumination angles with respect to the *w* component of velocity. The function $\Psi(\beta_{eff})$ is found by calibrating the model against the experiments of Castro[6] for flow normal to a perforated plate.

Figures 20 and 21 compare the experimental mean velocity measurements with the results obtained using the proposed body force method. The wedge considered has a half-angle of $\alpha = 20^o$ and porosity $\beta = 0.5$ and the nozzle pressure ratio is NPR = 2.0. These conditions closely resemble the operating conditions of wedge-shaped fan flow deflector installed in an actual turbofan nozzle. For a negative freestream illumination angle $\theta_{i\infty} = -4^o$ the body force model accurately depicts the blockage of flow through the wedge, showing excellent agreement with the experimental results in Fig. 20. The difference in the contours near the wedge base, particularly the asymmetry, is due to the distortion of the experimental flow by asymmetric streamwise vortex formation over the upper edge of the flaps. The agreement is similar when the freestream illumination angle is positive $\theta_{i\infty} = 12^o$, shown in Fig. 21. In both cases, the shape inner and out shear layers along with the magnitudes of the velocity at the wedge base are resolved well, reflecting the fidelity of the model.

V. Conclusion

Experiments and computations were used to analyze the flow field of porous wedge-shaped deflectors used for jet noise reduction in turbofan engines. The results reveal that the illumination angle, defined with respect to the freestream flow, has a profound impact on the flow field through and around the porous surface. For negative freestream illumination angles, there is no direct path for the flow to pass through the surface. Instead, flow through the perforations is driven by the pressure difference across the surface. This results in a low-velocity and nonuniform base flow that is undesirable for noise reduction. If the freestream illumination angle is positive, there is a direct path for incoming flow to pass through the porous surface resulting in higher magnitude and more uniform velocity distribution at the wedge base. This feature can be exploited by increasing the aspect ratio of the perforations in the streamwise direction and may prove valuable in the engineering of flaps with superior noise benefit and aerodynamic performance. A body force model is proposed which accounts for the effects of both porosity and illumination angle. Initial results show good agreement with experimental velocity measurements in wake of the wedge. The body force model provides a computationally feasible approach to simulating flow field of full turbofan nozzle equipped with porous wedge-shaped deflectors.

Acknowledgment

The support by NASA Cooperative Agreement NNX07AC62A (monitored by Dr. K.B.M.Q. Zaman) is gratefully acknowledged.

References

1. Papamoschou, D., Debiasi, M., "Directional Suppression of Noise from a High-Speed Jet," *AIAA Journal*, Vol. 39, No. 3, 2001, pp. 380-387.
2. Nielsen, P. and Papamoschou, D., "Mean Flow-Acoustic Correlations for Dual Stream Asymmetric Jets," AIAA-2009-0853, January 2009.
3. Papamoschou, D., "Fan Flow Deflection in Simulated Turbofan Exhaust," *AIAA Journal*, Vol. 44, No. 12, 2006, pp. 3088-3097.
4. Papamoschou, D., "Pylon Based Jet Noise Suppressors," *AIAA Journal*, Vol. 47, No. 6, 2009, pp. 1408-1420.
5. Mayoral, S. and Papamoschou, D., "Effects of Source Redistribution on Jet Noise Shielding," AIAA-2010-0652, January 2010.
6. Von Tanner, M., "Determination of Base Drag with Application to Near Wake of Wedges," Mitteilungen aus dem Max-Panck Institut für Strömungsforschung und der Aerodynamischen Versuchsanstalt, No. 31, Göttingen, 1964.
7. Papamoschou, D., Vu, A. and Johnson, A., "Aerodynamics of Wedge-Shaped Deflectors for Jet Noise Reduction," AIAA-2006-3655, June 2008.
8. Papamoschou, D., Zill, A. and Johnson, A., "Supersonic Flow Separation in Planar Nozzles," *Shock Waves*, Vol. 19, No. 3, 2009, pp. 171-183.
9. Sozer, E., Shyy, W. and Thakur, S., "Multi-Scale Porous Media Modeling for Liquid Rocket Injector Applications," AIAA-2006-5044, July 2006.
10. Xiong, J., Liu, F. and Papamoschou, D., "Computation of the Flow of a Dual-Stream Jet with External Solid and Perforated Wedge Deflectors for Noise Reduction," AIAA-2010-4863, June 2010.
11. Castro, I.P., "Wake Characteristics of Two-Dimensional Perforated Plates Normal to an Airstream," *Journal of Fluid Mechanics*, Vol. 46, No. 3, 1971, pp. 599-609.
12. Jameson, A., Schmift W. and Turkel, E., "Numerical Solutions of the Euler Equations by Finite Volume Methods Using Runge-Kutta Time Stepping Scheme," AIAA-1981-1259, January 1981.
13. Menter, F.R., "Two-Equation Eddy-Viscosity Turbulence Models for Engineering Applications," *AIAA Journal*, Vol. 32, No.8, 1994, pp. 1598-1605.
14. Xiong, J., Nielsen, P.E., Liu, F. and Papamoschou, D., "Computation of High-Speed Coaxial Jets with Fan Flow Deflection," *AIAA Journal*, Vol. 48, No. 10, 2010, pp. 2249-2262.
15. Liu, F. and Zheng, X., "A Strongly Coupled Time-Marching Method for Solving the Navier-Stokes and k-ω Turbulence Model Equations with Multigrid," *Journal of Computational Physics*, Vol. 128, No. 10, 1996, pp. 257-284.

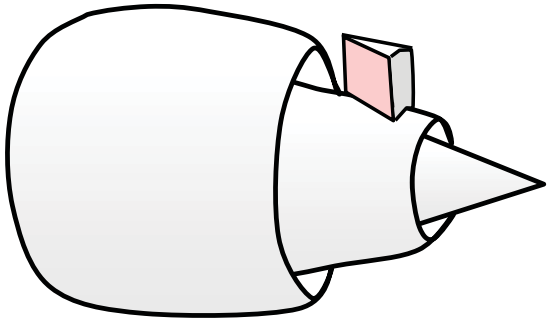

Fig. 1 Illustration of Fan Flow Deflection (FFD) wedge.

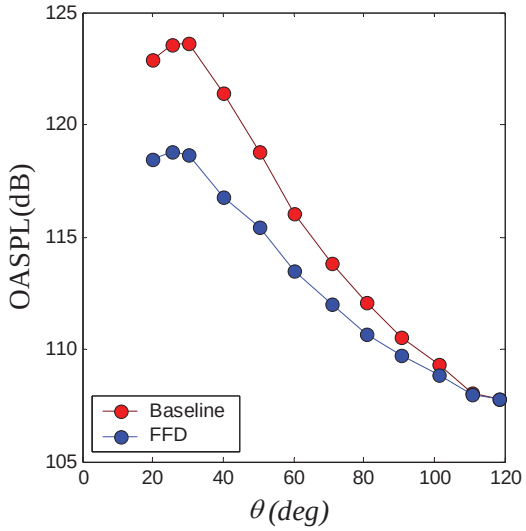

Fig. 2 Overall Sound Pressure Level versus polar angle from jet centerline.

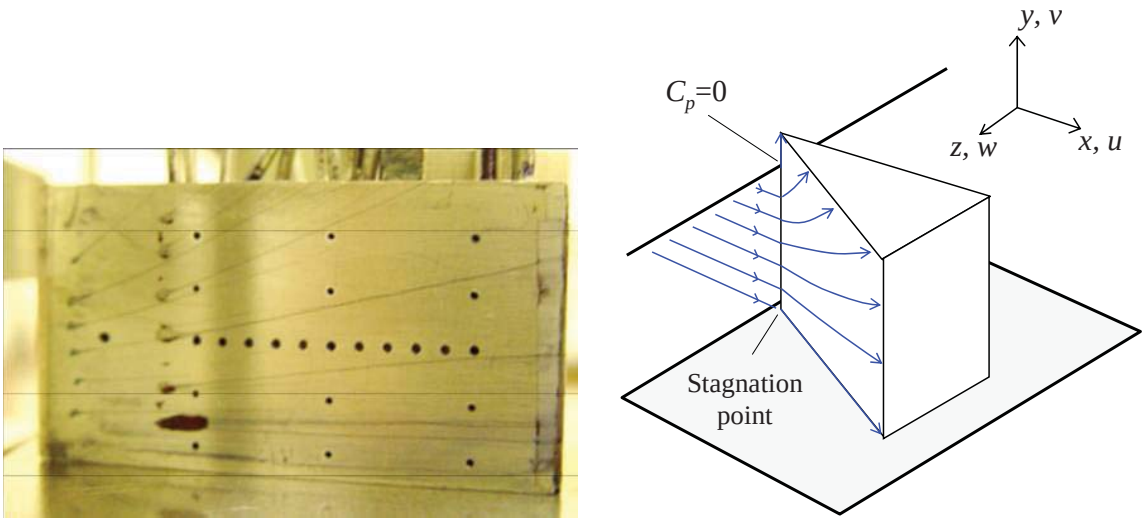

Fig. 3 Streak line visualization and schematic of flow field around FFD wedge.

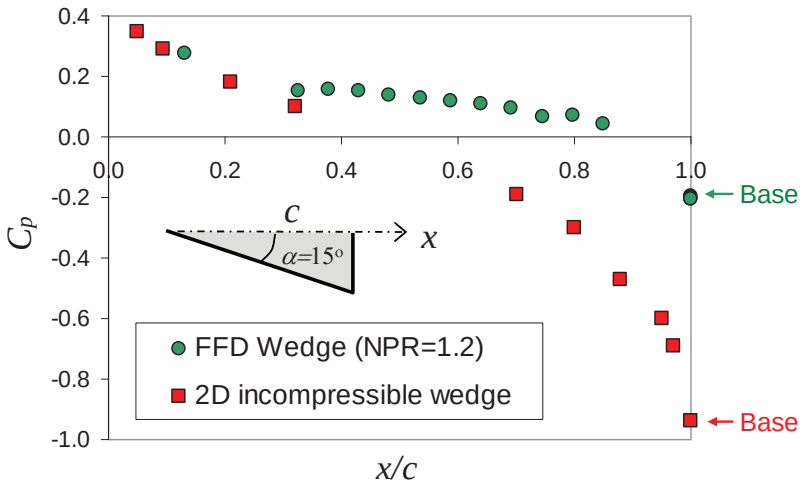

Fig. 4 Comparison of the surface pressure distribution between a classic 2D wedge and the FFD wedge.

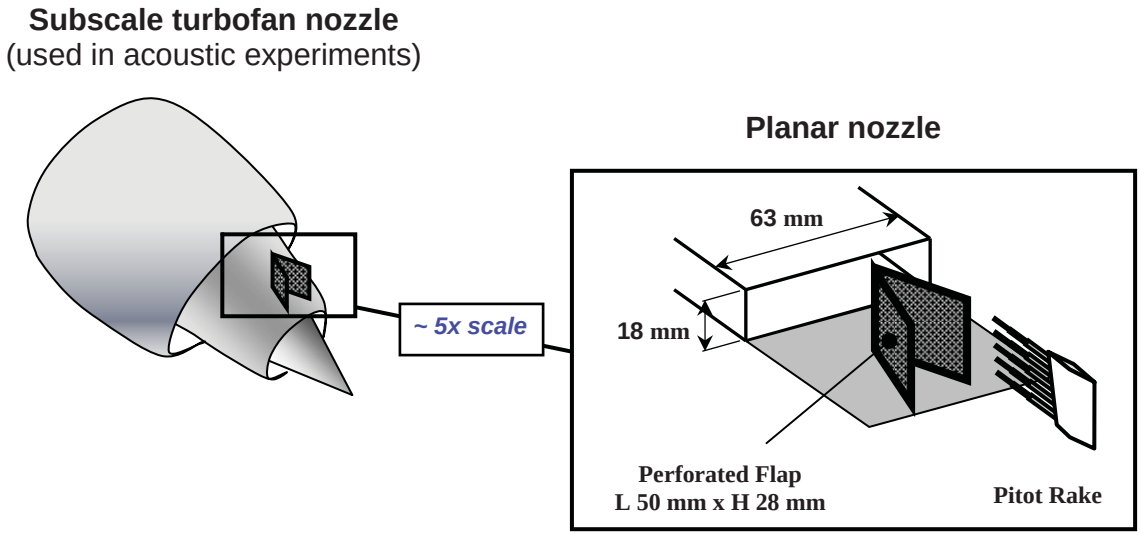

Fig. 5 Schematic of the experiment.

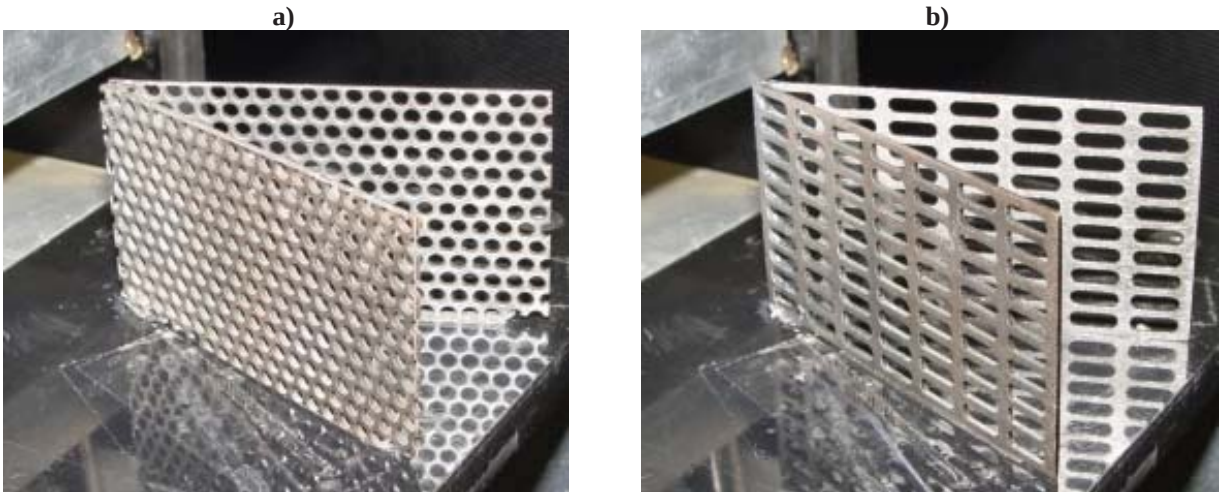

Fig. 6 Experimental perforated flaps with (a) AR = 1.0 holes and (b) AR = 3.0 holes.

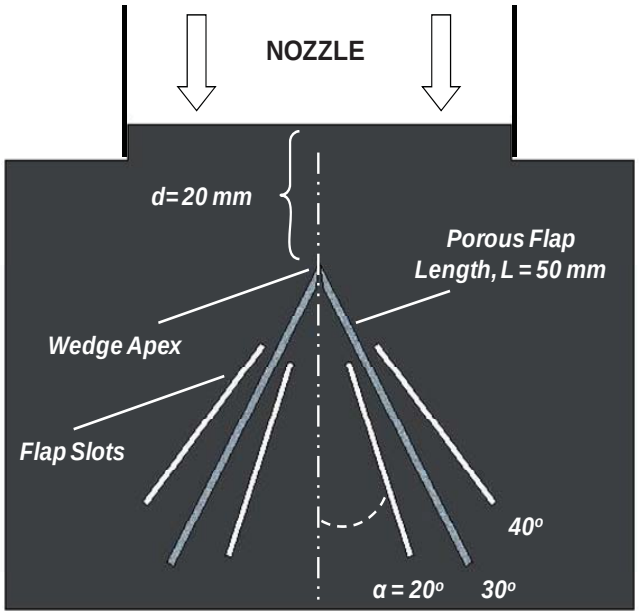

Fig.7 Top view of mounted flaps with relevant parameters shown.

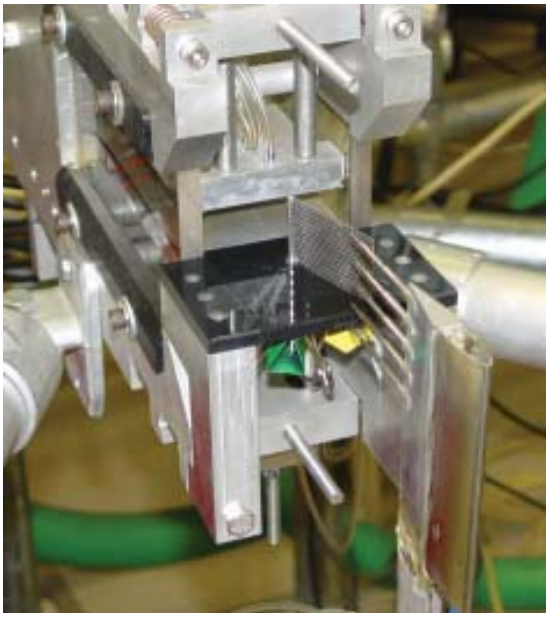

Fig. 8 Photograph of the experimental setup.

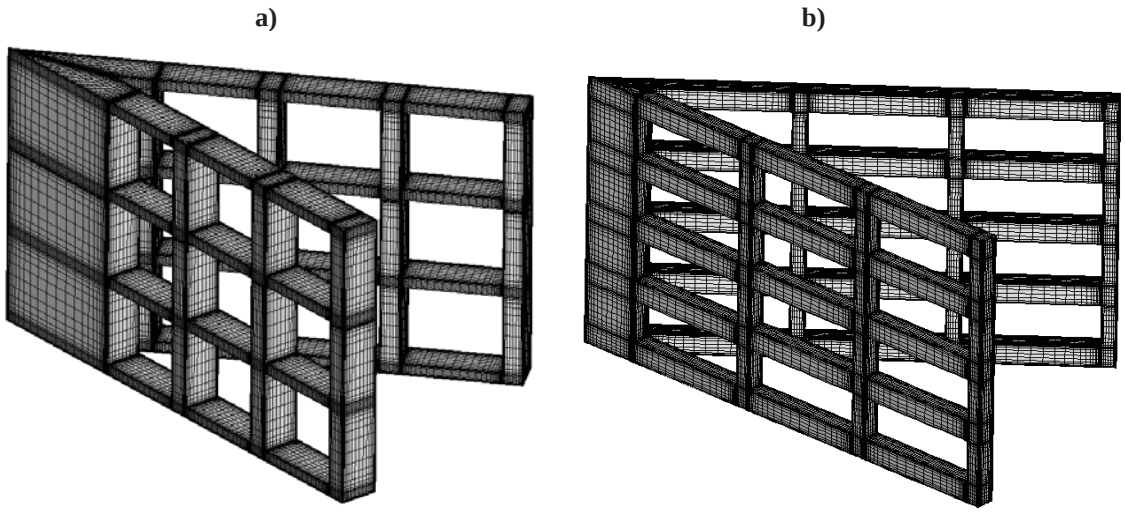

Fig. 9 Computational wedges with simplified geometries. a) AR≈1.0; b) AR≈3.0

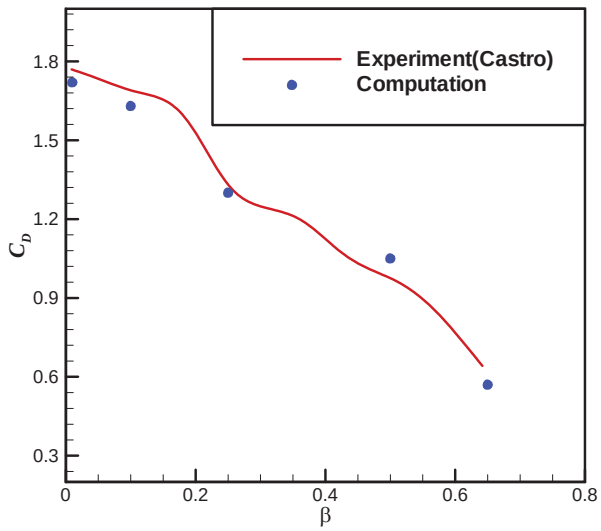

Fig. 10 Drag coefficient versus porosity for a normal perforated plate.

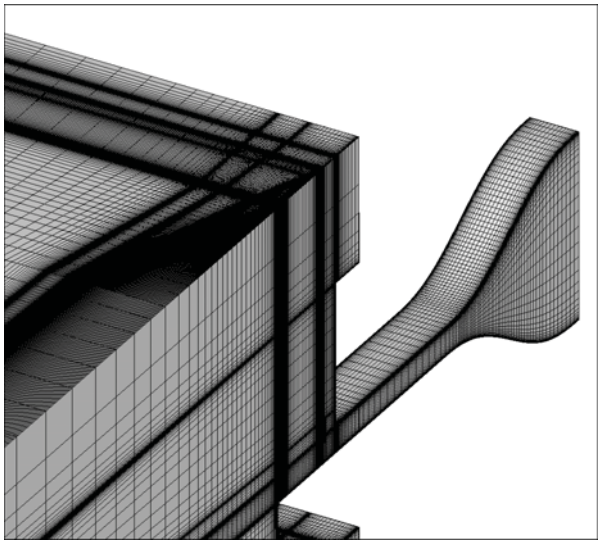

Fig. 11 Computational grid.

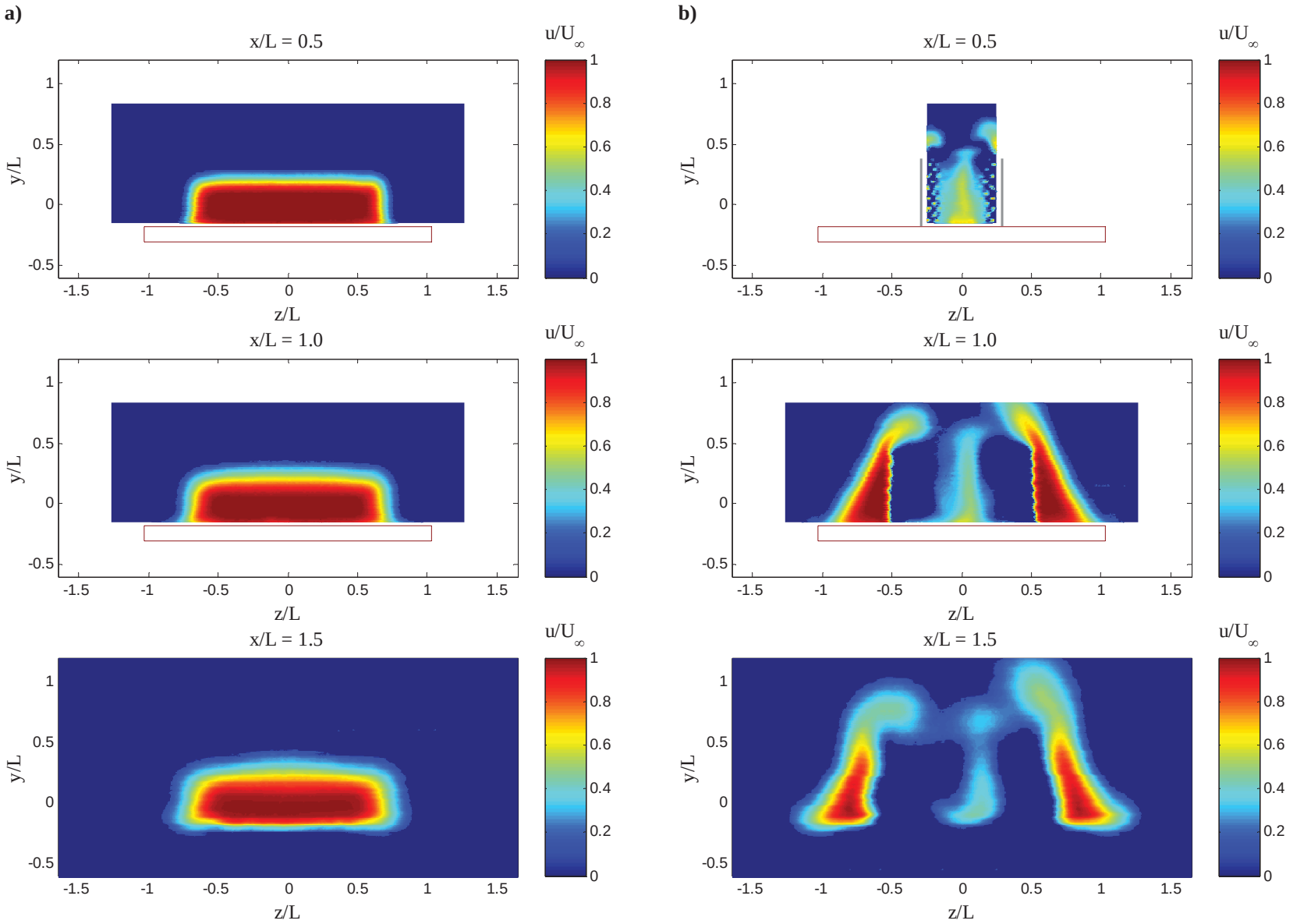

Fig. 12 Mean axial velocity contours at the first three axial stations for NPR = 1.6. a) No flaps; b) flaps with β = 0.5 and α = 30°.

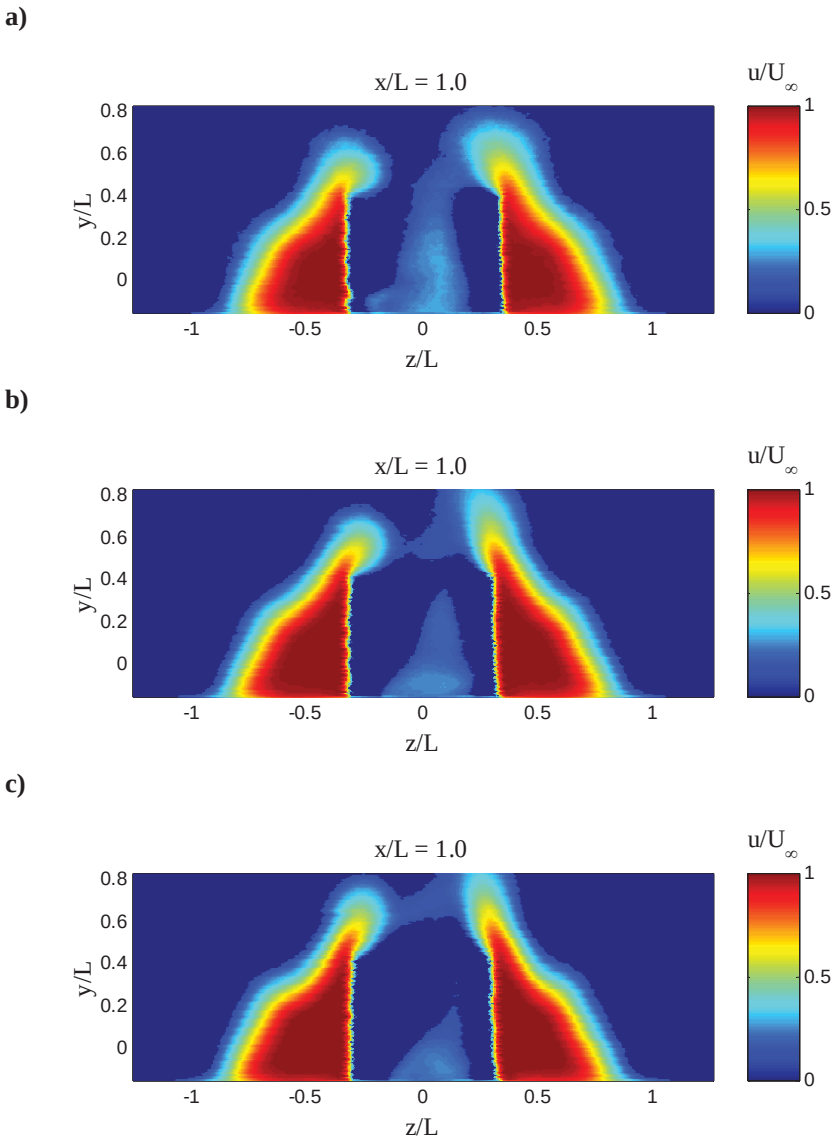

Fig. 13 Mean axial velocity contours at the wedge base for β = 0.5, α = 20^o and a) NPR = 1.2; b) NPR = 1.6; c) NPR = 2.0.

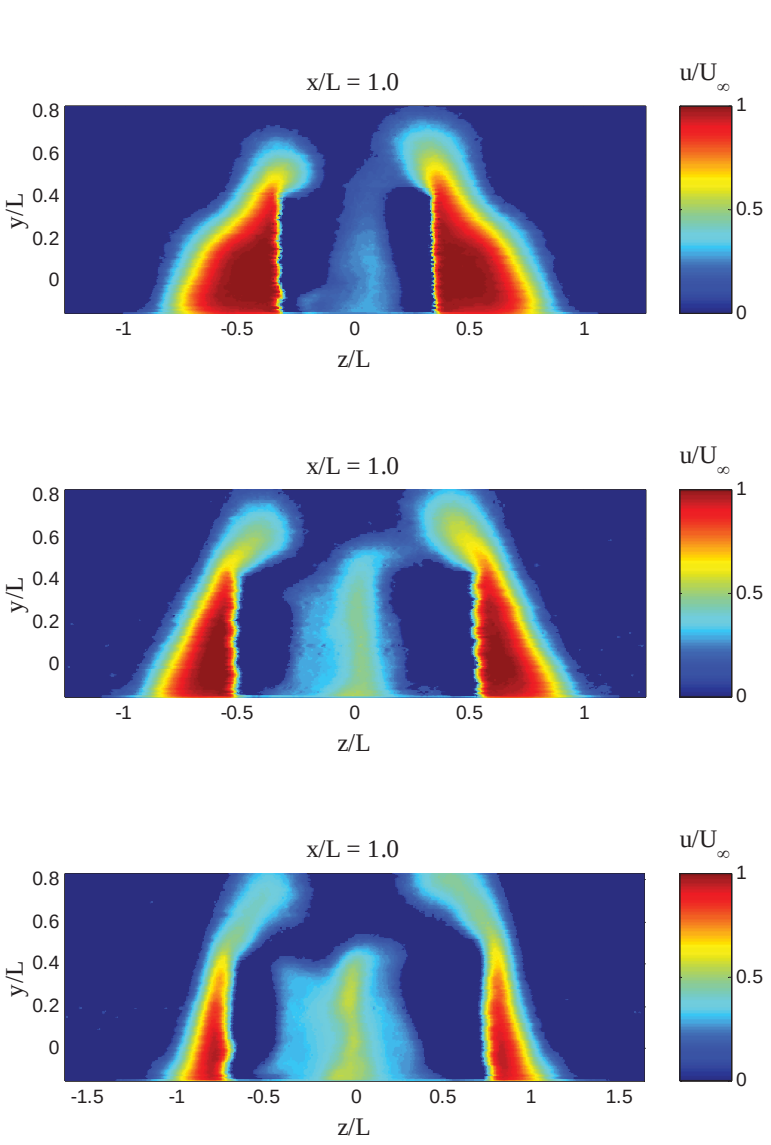

Fig. 14 Mean axial velocity contours at the wedge base for NPR = 1.2, β = 0.5 and a) α = 20^o; b) α = 30^o; c) α = 40^o.

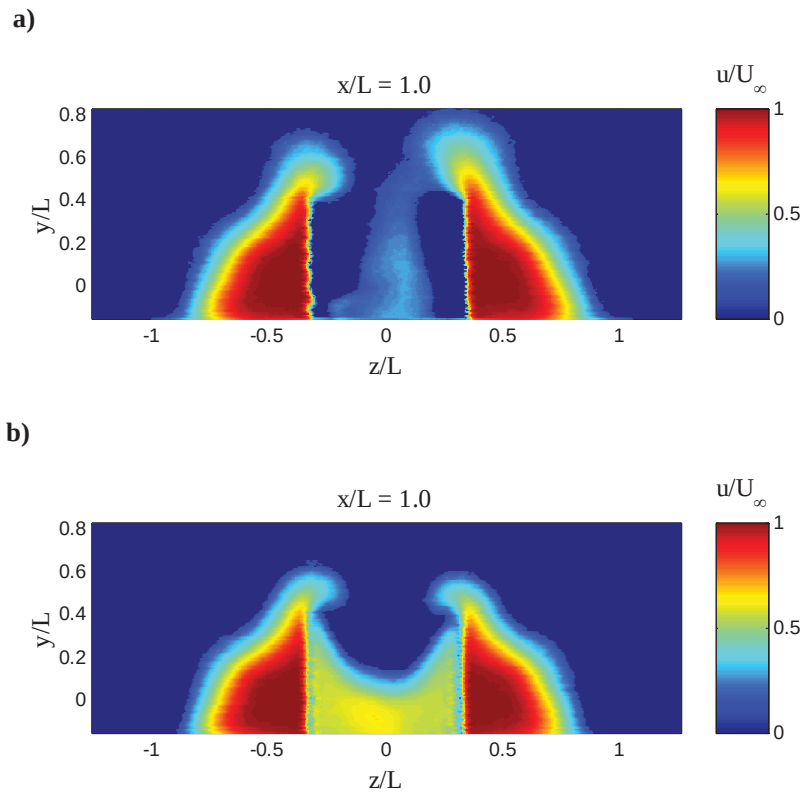

Fig. 15 Mean axial velocity at the wedge base for NPR = 1.2, β = 0.5, α = 20° and a) AR = 1.0; b) AR = 3.0.

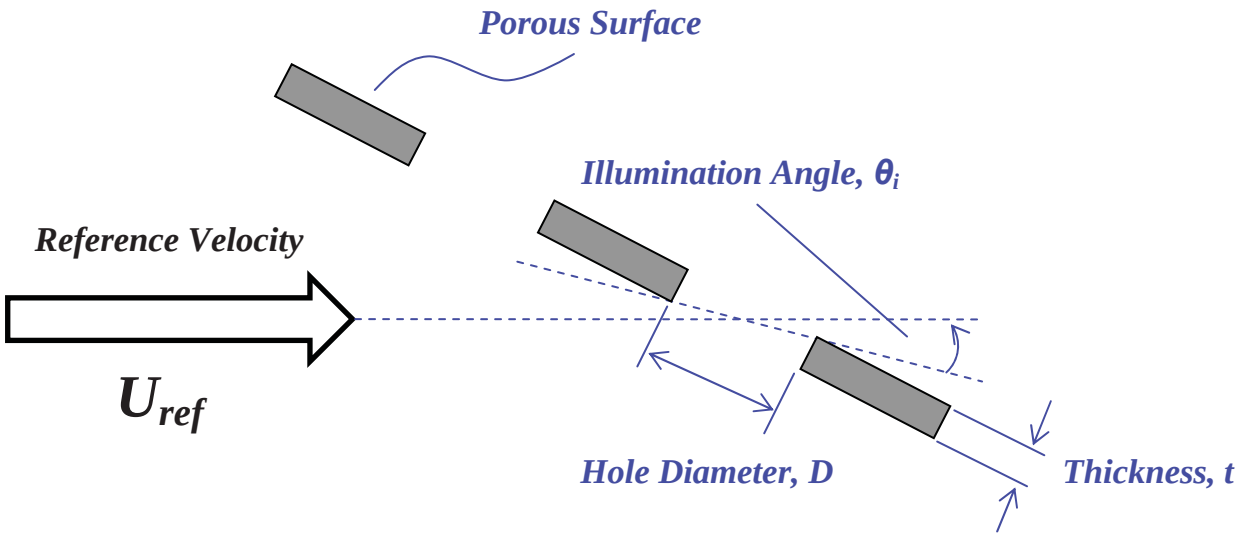

Fig. 16 Definition of illumination angle θ_i.

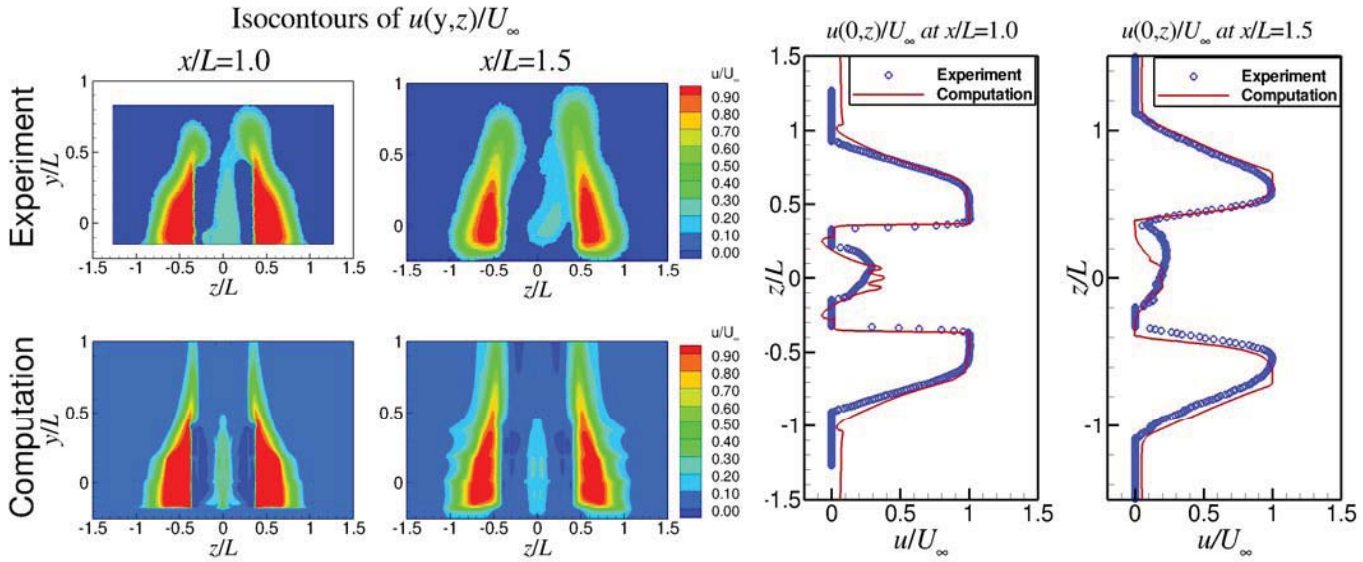

Fig. 17 Comparison of experimental and computational results for NPR = 1.2, β = 0.5, α = 20^o and $\theta_{i\infty}$ = -4^o.

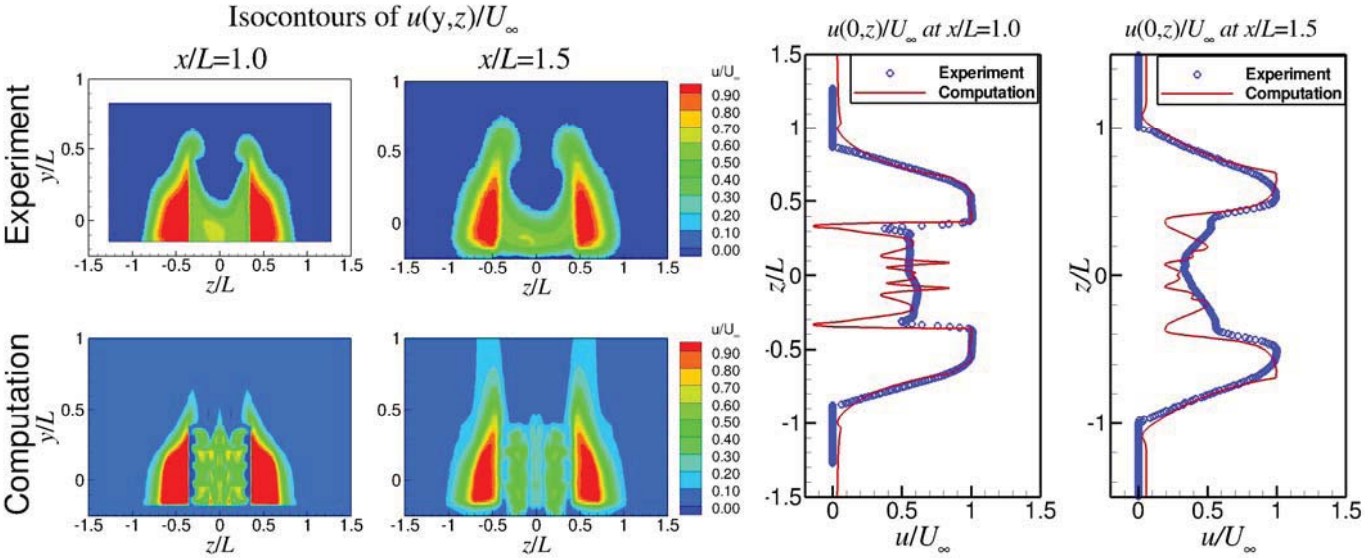

Fig. 18 Comparison of experimental and computational results for NPR = 1.2, β = 0.5, α = 20^o and $\theta_{i\infty}$ = 12^o.

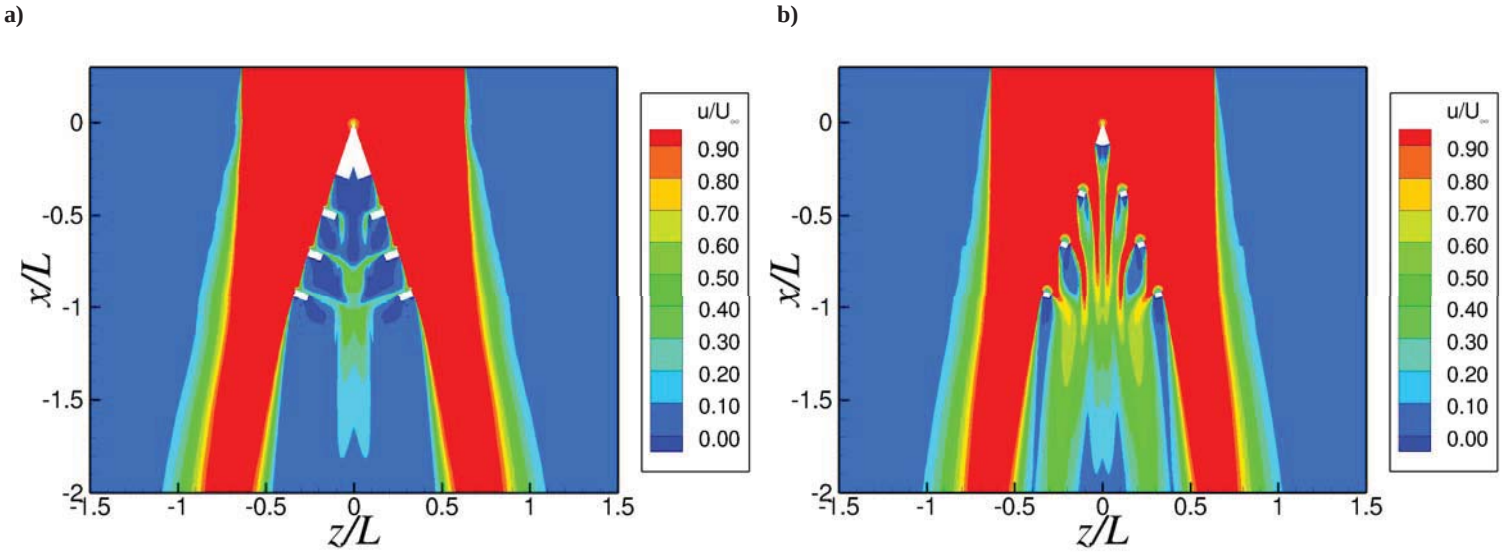

Fig. 19 Computational mean axial velocity in the *x*-*z* plane for a) $\theta_{i\infty}$ = -4° and b) $\theta_{i\infty}$ = 12° .

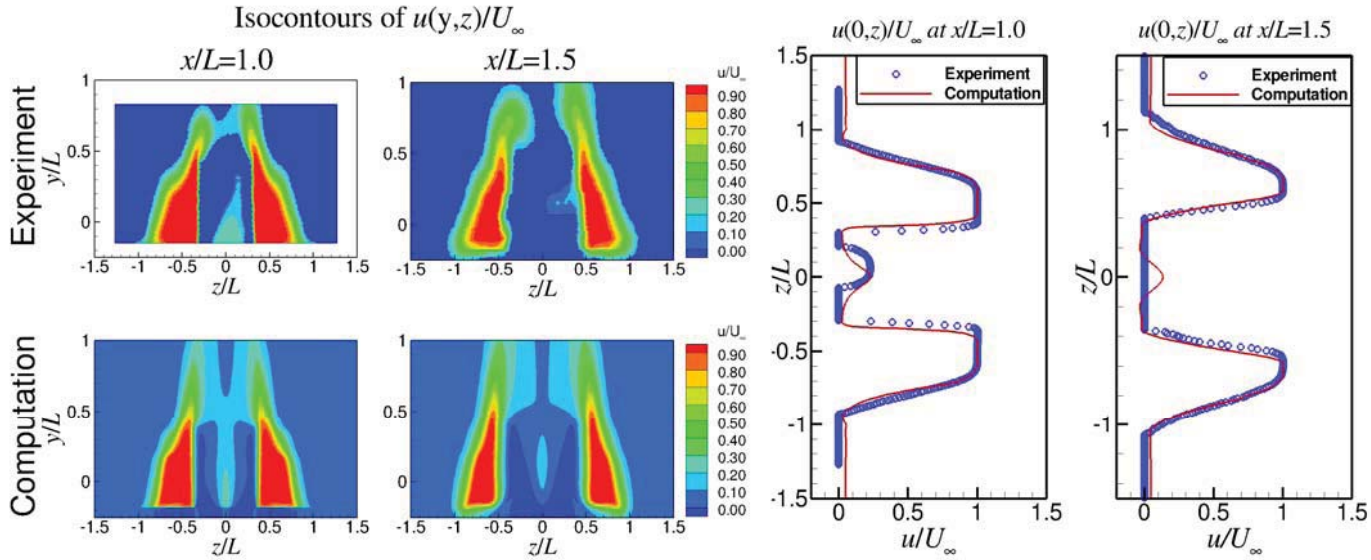

Fig. 20 Comparison of experimental and body force model results for NPR = 2.0, β = 0.5, α = 20° and $\theta_{i\infty}$ = -4°.

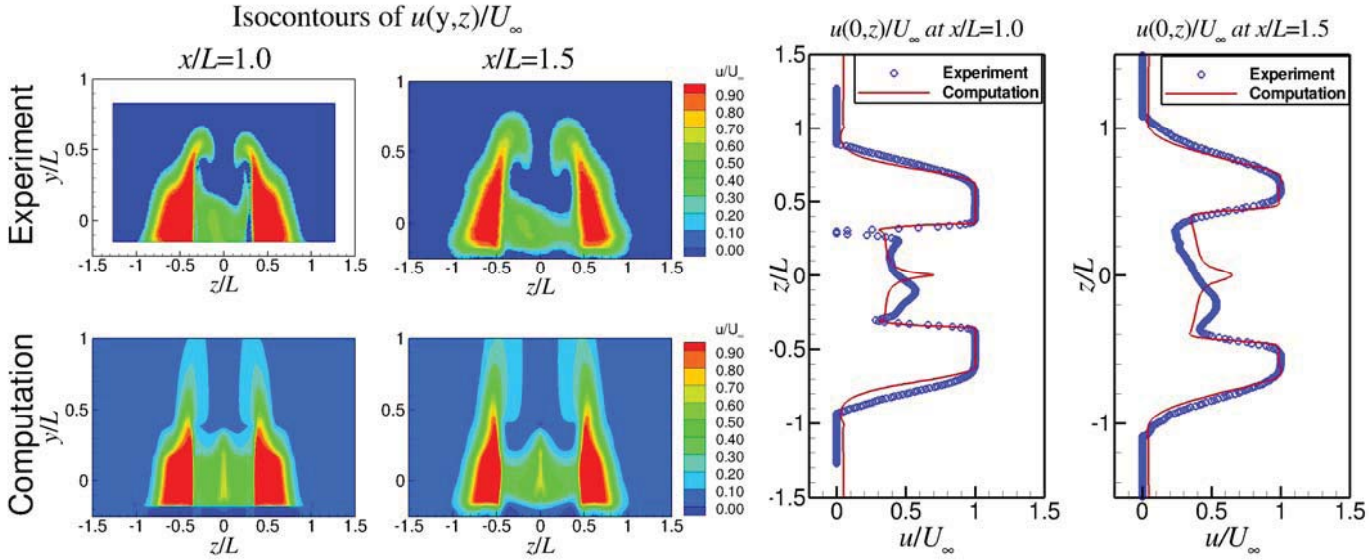

Fig. 21 Comparison of experimental and body force model results for NPR = 2.0, β = 0.5, α = 20° and $\theta_{i\infty}$ = 12°.